Article:

Microstructure of Conductive Binder Domain for Electrical Conduction in Next-Generation Lithium-Ion Batteries

Xuesong Lu, Guo J. Lian, Ruihuan Ge, James Parker, Milan K. Sadan, Rachel Smith, and Denis Cumming*

The purpose of this work is to investigate the structure and mechanism of long-range electronic contacts which are formed by wet mixing and their interaction and relationship with the structure responsible for ion transfer within the conductive binder domain of next-generation $LiNi_{0.6}Mn_{0.2}Co_{0.2}O_2$ lithium-ion batteries. This article introduces a novel concept involving an efficient adapted structure model, which includes a bridge structure with two "nested" small and large pore systems, and an effective electrode conduction mechanism involving two "nested" percolation systems. The article also highlights a limitation in the improvement of the battery performance by percolation systems for electron transfer, which is restricted by pore systems for ion transfer through the ratio of electrical conductivity (σ) and ionic conductivity (κ) as $\sigma/\kappa = 10$. The findings of this article may provide valuable insight for formulation design and manufacturing of an optimal structure of the conductive binder domain for next-generation lithium-ion batteries.

1. Introduction

Lithium-ion batteries (LIBs) have changed people's lives and have wide applications for electronic portable devices, electrical vehicles, and energy storage devices.[1,2] The development and growing demand for electric vehicles and electronic devices has led to an increase in expectations for the product performance of batteries. As a result, the next generation of LIBs aims to achieve high energy density and power density while maintaining low cost.[3,4] The specific energy or energy density of LIBs should exceed $350\,Wh\,kg^{-1}$ or $750\,Wh\,L^{-1}$ at cell level to fully meet the demand for auto applications.[5] The cost goal for most auto manufacturers is $\$125\,kW\,h^{-1}$ for a battery pack.[6] Due to these requirements, nickel and manganese-rich $LiNi_xMn_yCo_zO_2$ (NMC_{xyz}) emerges as one of the promising cathode materials. It offers the potential for achieving high energy densities, inexpensive and safe batteries. $LiNi_{0.6}Mn_{0.2}Co_{0.2}O_2$ (NMC622) is a good choice for cathode materials due to its excellent performance, high capacity, and energy density, relatively low cost, good stability, and safety. This makes it suitable for providing power supplies for electric vehicles, portable power tools, and electric energy storage systems.[7] Manganese is plentiful, inexpensive, and safe in comparison with cobalt[8] and is responsible for stabilizing the crystalline structure of layered oxide while nickel provides high capacity. The energy density is determined by the mass ratio of active materials, but the power density is determined by the conductive binder domain (CBD) because the CBD highly influences the electron transfer rates through electrical conductivity with the electrode porosity and pore tortuosity.[9,10] In this work, we seek to optimize electrode formulations and new processing methods by exploring the electrochemical mechanisms in the electrode for developing the next-generation LIBs.

The electrical conductivity affects the performance of LIBs significantly, particularly rate performance in batteries.[11] However, the electrical conductivity of active materials is less than $1\,S\,m^{-1}$. The conductivity of $LiFeO_4$ (LFP) at room temperature is of the order of 10^{-8}–$10^{-3}\,S\,m^{-1}$[12]; the conductivity of $Li_{1-x}Ni_{1-y-z}Mn_zCo_yO_2$ is 10^{-5}–$1\,S\,m^{-1}$ over Li concentrations $x = 0.00$ to $x = 0.75$.[13] The poor conductive network causes a relatively high ohmic drop during discharge.[14] Therefore, conductive additives such as carbon black are added to the electrode to provide conductivity through point-to-point pathways and assist the electron transfer.[15–17] The electrochemical reaction in the electrode is strongly influenced by the electrical conductivity as well.[18] The inadequate electrical conductivity results in the structure degradation of active materials during charge–discharge cycling and contributes to polarization of the electrode, which negatively impacts the electrochemical activity of the material by altering the redox potential due to the associated rise in resistance.[19] The efficient electron-conducting networks carry the electrons between the intercalation sites and the external

X. Lu, G. J. Lian, R. Ge, J. Parker, M. K. Sadan, R. Smith, D. Cumming
Department of Chemical and Biological Engineering
University of Sheffield
Mappin Street, Sheffield S1 3JD, UK
E-mail: d.cumming@sheffield.ac.uk

X. Lu, R. Ge, M. K. Sadan, R. Smith, D. Cumming
Faraday Institution
Quad One, Harwell Campus, Didcot OX11 0RA, UK

circuit. Without these electron-conducting networks, the intercalation reaction cannot occur. In contrast, the optimized electronic networks minimize heat production arising from ohmic heating. Currently, there is a combination of long-range (to describe the electronic contact in the electrode over the range of 0.1–10 μm) and short-range (to describe the electronic contact in the electrode on the 1–100 nm) length scale electronic contact of conductive additive particles that could improve electronic conductivity. The long-range electronic contacts span between active material particles in the 0.1–10 μm range, forming the interconnected percolation network. The short-range electronic contacts are the nearest neighbor 1–100 nm length interaction between active material particles and the surrounding CBD.[20] The heterogeneity of the CBD filling the space among active material particles highly affects the LIB performance.[21–23]

However, there is still an argument regarding the dominant electronic contact impacting the performance of the LIBs. Morelly et al. and Dominko et al. supported that short-range contacts are more important because for Li-ion insertion to occur without excessive polarization, both the Li-ion and electron have to be available at the same location on the surface of active material particles.[24,25] On the contrary, Wang et al. supported that long-range contacts are more important because dry mixing caused a continuous coating of carbon black on the surface of NMC which blocked ionic transport and weakened the electronic connection between active material particles.[26] Bockholt et al. pointed out that the well-established short-range electrical contacts by dry mixing limited the battery performance at high C-rates due to missing long-range contacts so the re-establishment of long-range contacts is of high importance.[27] Bauer et al. used dry mixing of conductive additives to build the short-range contacts followed by wet mixing of conductive additives to build the long-range contacts to improve the battery performance.[28] Dry mixing for establishing short-range contacts has been studied extensively but the re-establishment of long-range contacts by wet mixing still needs further examination. This work will focus on wet mixing for generating long-range electronic contacts and in the future, the results will be compared with dry mixing for producing short-range electronic contacts in the electrode. For wet mixing, there are two different CBD structures: 1) bridge (to describe the structure of conductive binder domain as a bridge morphology to cross over the two or more active material particles) structure linking two active material particles like a bridge and 2) film structure covering the surface of the active materials. It has been demonstrated that the bridge structure can increase the conductivity by more than 950% and the film can only increase the conductivity by 220%.[29] The shortcoming of the film structure is that it decreases the effective interface between active material particles and electrolyte, which is a crucial parameter for the LIB performance.[30,31] It is deduced that more bridge structures and thinner film structures are preferred for the CBD. However, the current challenges are: 1) processing methods to increase the bridge structures; 2) identification of bridge and film structures; 3) mechanism of conduction in the electrode; and 4) limitation factors for electron transfer and the relationship between electron transfer and Li-ion transfer. The pore size and pore tortuosity in the electrode are critical for Li-ion transfer and small pore size and high pore tortuosity decrease the ion transfer rate.

NMC622 is a relatively new material for next-generation LIBs. It is different from other cathode-active materials, such as LFP, in that the particle size is much larger (around 10 μm) and a comparatively lower CBD mass fraction is required. Therefore, knowledge acquired by the traditional LFP system may not necessarily be applicable to systems with micron-scale active material morphology. Therefore, the aim of this article is to investigate the CBD structure formation mechanism which forms long-range electronic contacts during processing, and the mechanism of CBD electrochemistry in the electrode for the NMC622 system. Additionally, we aim to build the relationship between CBD structures, conductive additives, and the pore distribution. This contribution also explores the mechanism of conduction and conduction limitation by Li-ion transfer. Ultimately, the goal is to design the optimal formulation of the ratio of conductive additive and binder for next-generation LIB electrodes.

2. Result and Discussion

2.1. Rheological Properties of the Slurries

The rheological properties of slurry for coating highly affect the flow during the coating process and the microstructure after coating.[32] The slurry for coating is a shear-thinning and weakly binder-coagulated dispersed colloid gel system, exhibiting a power-law relationship with a mild yield point. The poly(vinylidene fluoride) (PVDF) and micron-sized NMC622 tend not to form a stable gel structure but the addition of carbon black helps to stabilize the NMC622 particles against fast sedimentation to form a stable slurry system.[33] The viscosity, storage modulus, and loss modulus increase with the solid concentration, and a time-dependent rheological behavior can be observed in creep and hysteresis loop experiments.[34] The solid content of the slurry for coating is recommended to be 64–66% by Ouyang et al.[35] because at this stage, a weak bridge flocculation network structure is formed. This structure can improve the dispersion uniformity and stability of the slurry without yield stress existing in the slurry and limit the particle and binder migration during drying.

The CBD structure, such as pore morphology and carbon binder distribution along the vertical direction to the current-collector, is highly influenced by the slurry colloidal interaction between PVDF, NMP, carbon black, and NMC622 through drying with particle aggregation and polymer migration driven by solvent evaporation.[36] Different colloidal interactions lead to different active material particle pile-ups with varying porosities. Furthermore, different carbon-binder forms different CBD structures such as sponges, bridges, and film, as well as the distribution of carbon-binder throughout the electrode. These colloidal interaction forces include van der Waals, steric, electrostatic, hydrodynamic, and depletion interaction based on Derjaguin–Landau–Verwey–Overbeek (DLVO) theory.[37] The rheological properties reflect the colloidal interactions.

In this work, the experimental results of shear rate sweeping and the relationships between viscosity and shear rate for different slurry formulations are shown in **Figure 1**. The experimental results of strain sweeping with a shear rate of $1 \, \mathrm{s}^{-1}$ and the
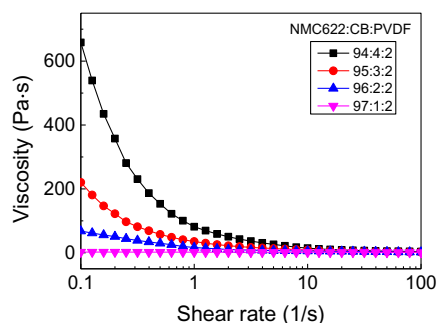
Figure 1. Relationship between viscosity and shear rate for different formulations.

relationships between storage/loss modulus and shear strain for different formulations are shown in **Figure 2**.

From Figure 1, the viscosity decreases from the formulation of 94:4:2 to 97:1:2. For example, at the shear rate of $1\,\mathrm{s}^{-1}$, the viscosity changes from 81.8, 35.3, 16.7 to 2.0 Pa·s for the formulation of 94:4:2 to 97:1:2, respectively. Simultaneously, from Figure 2, the storage modulus and loss modulus reduce from the formulation of 94:4:2 to 97:1:2. For example, at the strain of 1%, the storage modulus and loss modulus change from 236.7, 77.1, 53.0 to 0.3 Pa; from 162.8, 40.7, 33.1 to 1.8 Pa for the formulation of 94:4:2 to 97:1:2, respectively.

The above phenomena are caused by two reasons: 1) variation of carbon black content; and 2) variation of solid content in the slurry, but the critical factor is the carbon black content. Sung investigated the rheological properties of slurries, consisting of PVDF, carbon black, NMC111, and NMP, and found that carbon black and PVDF form a colloidal gel in the NMP solution.[38] High-volume fraction of large active material particles with

non-Brownian movement has little effect on the rheological properties of the slurry because NMC111 particles do not form the gel in the PVDF and NMP solutions. Therefore, carbon black dominates the rheological properties of the slurry. Currently, the mass ratio of carbon black to PVDF is 2:1, 1.5:1, 1:1 and 0.5:1 for formulation from 94:4:2 to 97:1:2, respectively, and the viscosity, storage/loss modulus decrease correspondingly. The ratio of carbon black to PVDF is crucial for coating and highly influences the CBD structure formation and final electrode performance. This conclusion will be demonstrated in the following sections.

Besides the effect on electrical conductivity, the content of carbon black in the slurry highly impacts the rheological properties of the slurry and the slurry colloidal gel formation. Because of that, it may further influence the formation of bridge structures and pore structures in the electrodes, and subsequently, electrical conductivity and Li-ion diffusion in the liquid electrolyte through the coating and drying processes. It is demonstrated in the following sections that high viscosity such as the formulation of 94:4:2 is conducive to forming bridges and low viscosity such as the formulation of 97:1:2 is conducive to forming films.

2.2. Identifying the Bridge Structures in the Electrode from Top View

The drying process is critical for forming CBD structures and undergoes four stages: 1) particle aggregation; 2) film consolidation; 3) film shrinkage and pore emptying; and 4) segregation and bonding.[39] It is known from the study of Zhang et al.[39] that the bridge structure should be formed during the drying of the carbon black and PVDF colloid at the stage of film shrinkage and pore emptying, and it is highly influenced by the slurry
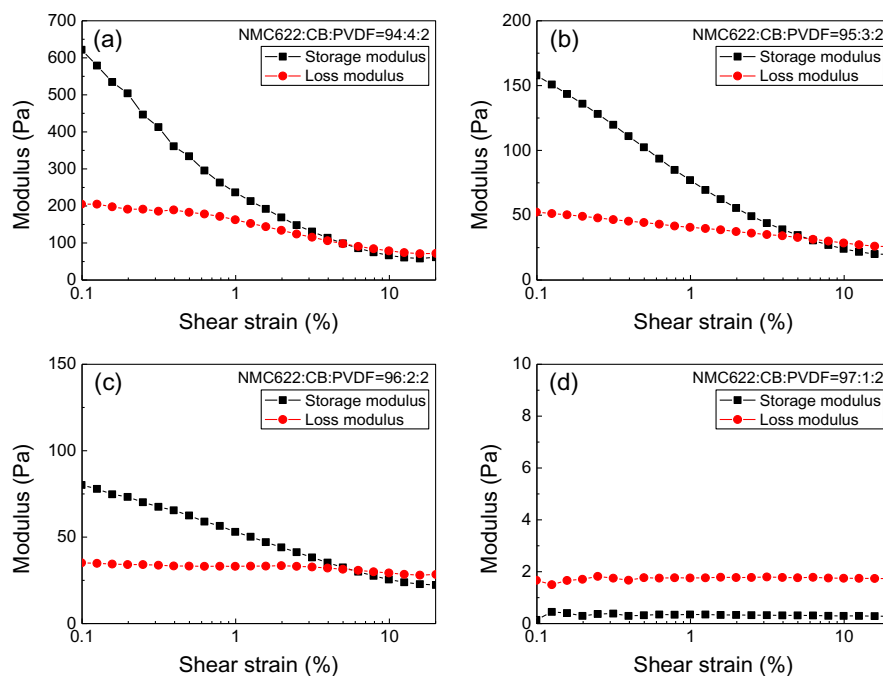
Figure 2. Storage modulus and loss modulus under strain sweeping and frequency sweeping for different formulations. a–d) 94–97 wt% active material, respectively.

**ADVANCED
SCIENCE NEWS**
www.advancedsciencenews.com

Energy Technology
Generation, Conversion, Storage, Distribution
www.entechnol.de

drying process. At this stage, with a low level of solvent and shrinkage of coating occurring, the solid constituents in the wet film will aggregate with each other to form a connected solid layer during shrinkage and the porous structure will form as the backbone of the dry film.[39] The bridge structure is generally forms around the contact point between two active particles, and thus it increases the contact area between active particles. Generally, the solid volume fraction in the colloid can increase from 22 to 33 vol%, and as high as 47 vol% with drying.[40] In contrast, maintaining a relatively high solid content in the colloid is favorable for forming the bridge structure. The possible reason is that the capillary force from dense particle pile-up may drive more carbon and binder moving to the particle contact area. Simultaneously, when the porosity of carbon black in CBD is approximately 67 vol%, which is the density of the porous CBD with small pores, the resistance and capacity loss reach the lowest value.[41] Therefore, the ideal solid fraction of carbon black in the dried CBD may be in the region of 33 vol%. This is a significant result because it represents the typical minimum volume fraction needed for a percolating network. This typical minimum carbon black needed for percolation was determined by Mayer et al.'s experiments with the lowest resistance and loss of capacity,[41] and the measured conductivity of the composite of binder and carbon black with different carbon black content in Section 2.5. The threshold of percolation is related to the relative volume percentage of the conductive phase and may change in the case of a different active material. This can be determined directly by measuring the conductivity of a film as a function of the conductive additive content. At a CBD content below approximately 4 wt%, the electronic conductivity drops substantially, which is demonstrated in Sections 2.5 and 2.8. Slurry casting leads to a porous CBD phase with small pores, resembling a "fluffy" or "sponge-like" structure. This CBD phase is estimated to be roughly 60% porous in a typical electrode. Therefore, the volume of the CBD that is less than 3 wt% corresponds to slightly less than 30 vol%, which is the typical knee in a percolation S-curve. Here, the "nested" (to describe the interaction between two percolation systems and two pore systems) small pore and large pore system results in "bridging" structures between active material particles and therefore confers long-range conductivity in an electrode.

The SEM images shown in **Figure 3** are similar due to the large micron-sized active material particles of about 10 μm. Additionally, the area and volume occupied by the CBD are relatively small because of the relative lower mass fraction of PVDF and carbon black. However, upon closer examination of the CBD near the contact point between two active material particles, the subtle differences among these SEM images can be identified. These SEM images shown in Figure 3 (a–d: magnification 1,000; e–h: magnification 5,000) demonstrate that there are two types of CBD structures: bridge and film. Schematic diagrams are provided in Figure 3i–l to guide and assist in interpreting these observations. The bridge fills the space between two NMC622 particles or the space among several NMC622 particles. Generally, the bridge structure is located around the contact point of active particles. In contrast, the film covers the surface of the active particles. The mass quantity of carbon black highly influences the CBD structures. As shown in Figure 3, with increasing mass quantity of carbon black from 0.15 to 0.60 g in the formulation, the number of CBD bridge structures increase and become more clearer, as shown in SEM images from Figure 3d,h to a,e, and the schematic diagrams from Figure 3l to i which were generated based on SEM images and the study of Mayer et al.[41] The bridge structures contribute to electrical conductivity more than film.[29]
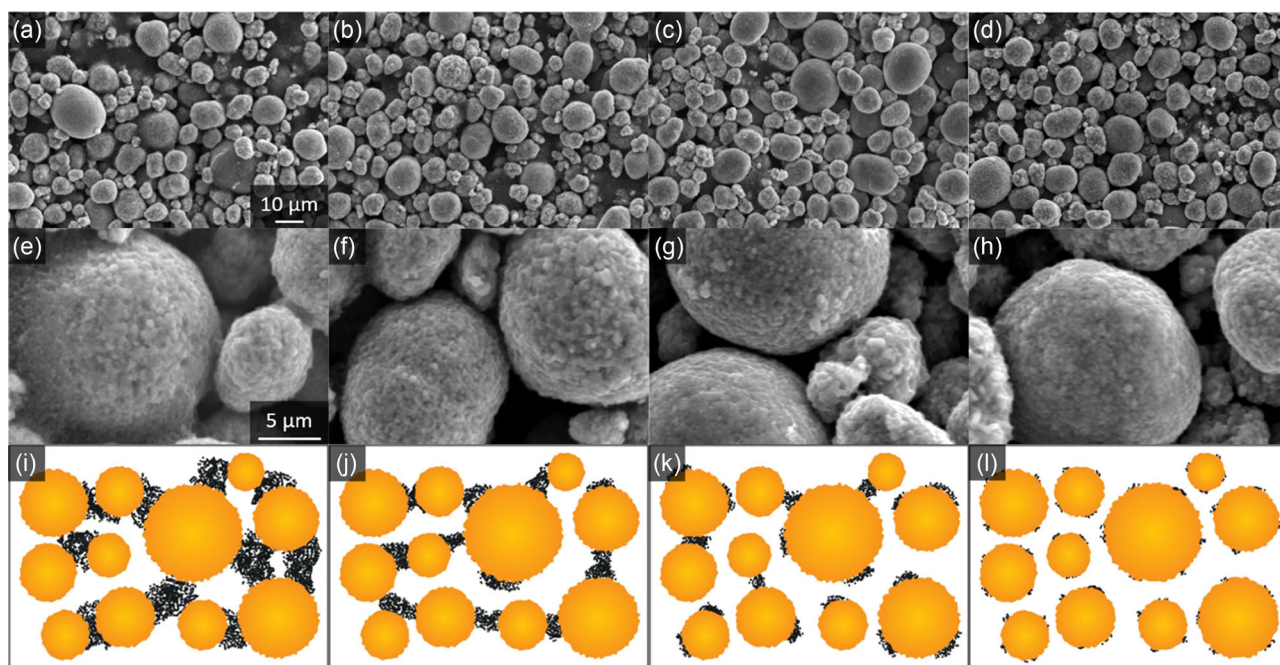
Figure 3. SEM images and schematic diagram of electrodes prepared from formulations (NMC622: carbon black: PVDF) a,e,i): 94:4:2; b,f,j): 95:3:2; c,g,k): 96:2:2; d,h,l): 97:1:2.
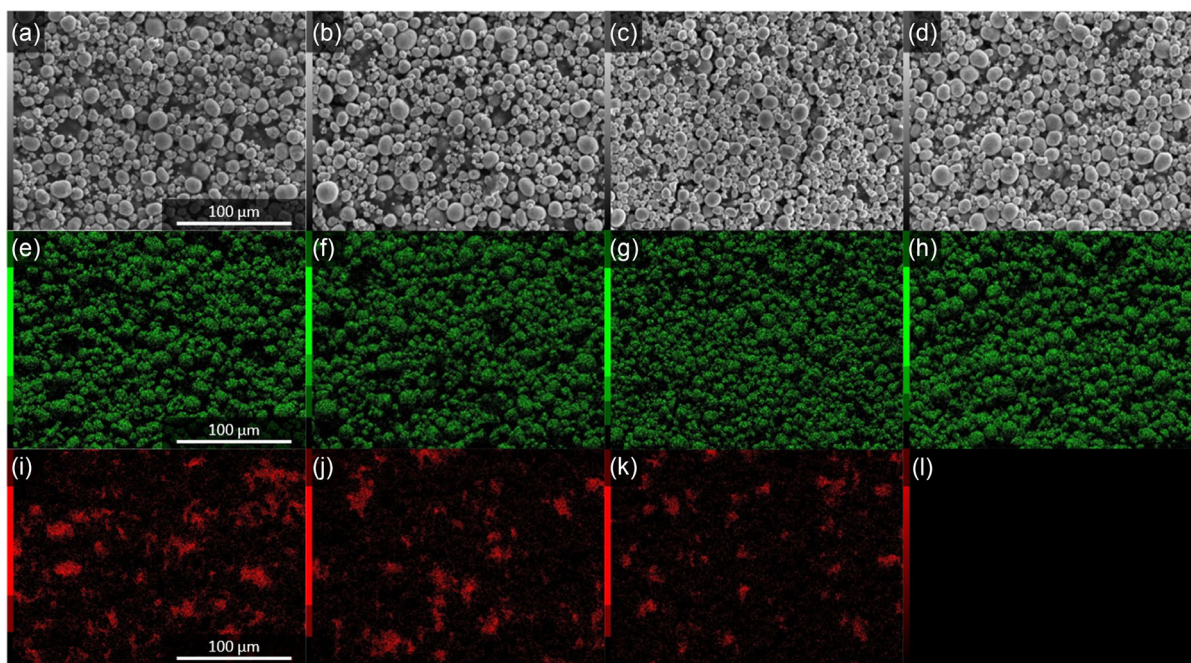
Figure 4. SEM images of element mapping areas a–d) and EDS carbon mapping of electrodes prepared from formulations (NMC622: carbon black: PVDF) a,e,i) 94:4:2; b,f,e) 95:3:2; c,g,k) 96:2:2; d,h,l) 97:1:2. Oxygen mapping: (e–h). Carbon mapping: (i–l).

2.3. Identifying the Carbon Distribution through EDS Carbon Mapping

Figure 4 shows the elemental mapping of the top surface of the electrodes. Due to the rough surfaces, quantitative mapping cannot be performed, but a relative quantitative comparison is possible. Oxygen mapping represents the NMC622 particle distributions and NMC622 particles are distributed evenly over the entire field of view. Due to the collection physics of low energy peaks, a degree of topography can also be seen in the O K-edge maps. CBD bridge structure distributions are clearly visible in the carbon map. The distribution of carbon black is not uniform, which could be used as a proxy metric for long-range electronic contacts. It is noticeable that some areas have a greater concentration of carbon black while others have a lesser concentration, likely associated with carbon-binder migration during drying. The small red areas can be regarded as "bridge" structures between NMC622 particles. The EDS carbon mapping also shows more carbon black in the electrodes from the right image (formulation: 97:1:2) to the left image (formulation: 94:4:2), and more carbon bridges and clusters appear.

2.4. Identifying the Bridge Structures in the Electrode from Cross-Section

The microtome was used to prepare cross-sections of the electrode to observe the CBD structures from a cross-section view. The SEM images of electrode cross-sections (formulation 95:3:2) before calendering are shown in **Figure 5**. These SEM images display a near-smooth 2D plane of the electrode. However, due to the angle of the blade, some

particles on the NMC622 polished surface were pulled off during cutting.

It is challenging to distinguish between the resin and CBD from Figure 5, but the CBD is mainly concentrated on the contact point between two active material particles while the resin surrounds them. Due to the difference in structure and conductivity between resin and the CBD, the subtle differences can be still identified under SEM. To clearly distinguish the resin and CBD, white dotted lines were added to the SEM images. In Figure 5, the large, white spherical particles are NMC622 particles while the CBD corresponds to the rough, irregular gray area near the particle, surrounded by the white dot line and the particle itself. The smooth gray area far around the particle, representing the periphery of the white dot lines, is the support resin that has filled the macropores within the electrode. In regions where the NMC622 particles are aggregated, it is more likely to adsorb more PVDF. This phenomenon occurs due to the drying process, where the volatilization of the solvent and the action of surface tension take place. As a result, PVDF is more likely to move to the capillary formed by the aggregation of the particles causing PVDF to be attracted around the particles. The drying model can be referred to in the reference article published by Nikpour et al.[36]

It is clearly shown in Figure 5a,b that a large amount of CBD appears in the voids formed by particle aggregation. As shown in Figure 5c and the upper region of Figure 5d, the PVDF is present because of the voids where particle aggregation occurs. Therefore, in these regions, PVDF is attracted by the capillary force leading to the formation of CBD around NMC622 particles.

Through the SEM images, it can be further verified that the CBD is predominantly distributed in the large pores where the particles gather.

ADVANCED
SCIENCE NEWS

www.advancedsciencenews.com

Energy Technology
Generation, Conversion, Storage, Distribution

www.entechnol.de
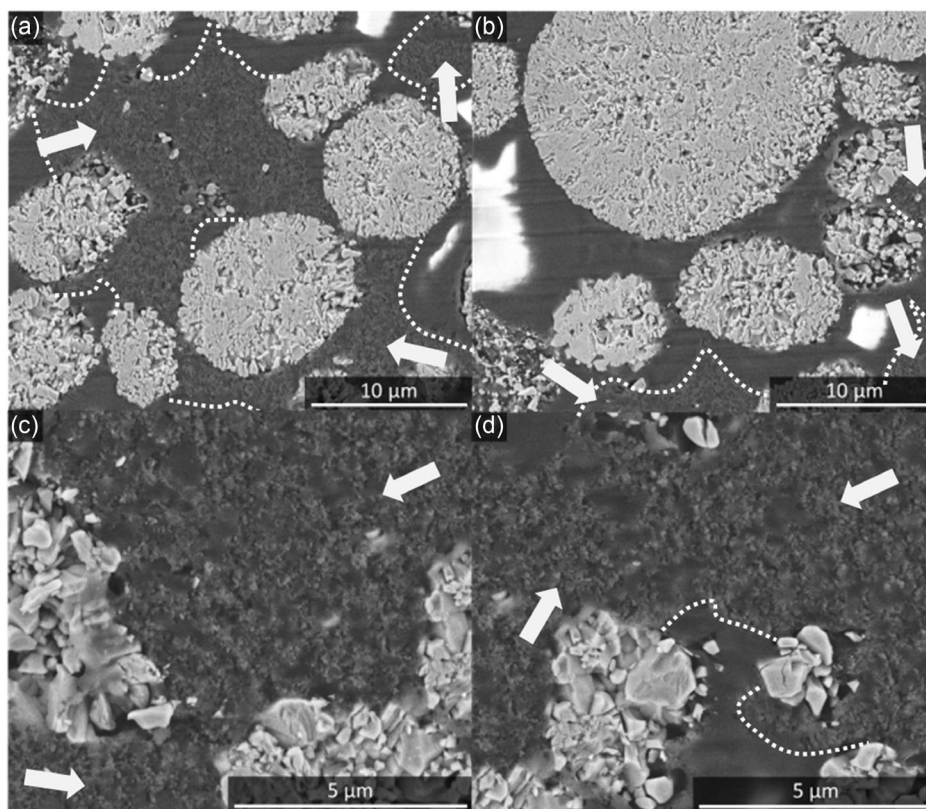
Figure 5. SEM images from the cross-section of the electrode (formulation: 95:3:2) prepared by resin filling and microtome. a,b) Magnification 10 000; c,d) magnification 30 000. White arrows indicate regions where the CBD is present.

This leads to the revelation that a denser particle packing should be formed prior to or during the coating and drying process to promote the formation of CBD bridge structures. The possible methods are: 1) to use the roller spreading dry particles and binder jetting additive manufacturing to obtain the dense film before drying; 2) to control the distribution of NMC622 particle size to reduce the porosity; 3) to avoid the slurry turning into a strong gel before coating; and 4) to calender the coated film before it is completely dried. These will be investigated or demonstrated in further research.

2.5. Electrical Conductivity and Two-Nested Percolation Systems for CBD in the LIB Electrode

To establish the nature of the conduction in the CBD, several compositions containing only carbon black and PVDF were prepared and measured by the four-point method. The electrical conductivity (σ) can be described by the following equation

$$\sigma = \frac{I}{\ln(2)\Delta V \cdot t} \tag{1}$$

where I is the current between the two outer probes; ΔV is the voltage between the two inner probes; t is the thickness of the coating. Conduction of the carbon black in PVDF can be described by the classical percolation theory. The general equation for a percolation universal law[42] is

$$\sigma = \sigma_0 (V - V_c)^s \tag{2}$$

where σ_0 is the conductivity of the carbon black; V is the volume fraction of the carbon black; V_c is the volume percolation of threshold concentration; and s is a constant. The relationship between σ and V is described by an S-shaped curve.

The electrical conductivity of the carbon black in PVDF is shown in **Figure 6**a. It shows that the threshold volume fraction for carbon black dispersed in PVDF is around 20 vol%. If carbon black continues to be added to the PVDF, the S-shape percolation curve will be shown and the electrical conductivity eventually approaches the conductivity of the pure carbon black.[43] However, the S-shape curve is a theoretical curve. In reality, a very high quantity of carbon back and a very low quantity of binder cannot form a stable film, such as 95 vol% carbon black with 5 vol% binder. Because of that, it is difficult to experimentally measure the conductivity of the film with a high volume of carbon black (i.e., more than 70%) and a low quantity of binder (i.e., less than 30%). The reason is that the binder does not fully fill the free space between the carbon black, and it may introduce air within the film. This phenomenon may lead to lower measured conductivity.

The curve in Figure 6a from this work is similar to the curve from the study of Liu et al.[44] The carbon black volume fraction in the composite of carbon black and PVDF for the formulations of (in wt%) 94:4:2, 95:3:2, 96:2:2, and 97:1:2 corresponds to 69.0, 62.5, 52.7, and 35.7 vol%. The corresponding electrical
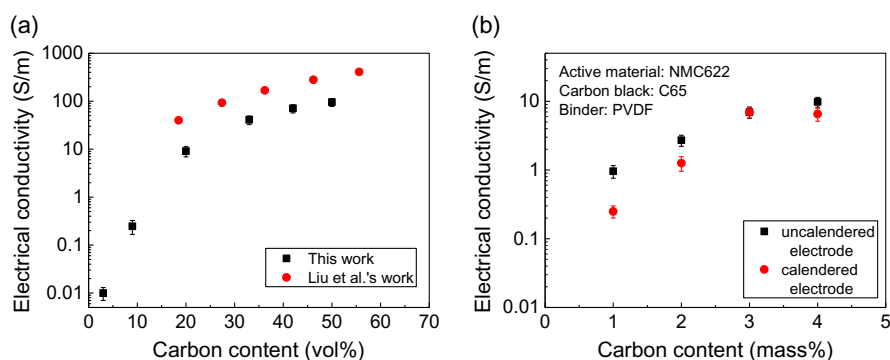
Figure 6. Electrical conductivity of carbon black in PVDF and electrodes a) composites of carbon black and PVDF in comparison with ref. [44]; b) NMC622 electrodes.

conductivity of composites (carbon black and PVDF) can be obtained from Figure 6a. In all cases, the volume fractions of carbon black are higher than the threshold volume fraction.

To measure the electrical conductivity in real electrode films, the slurry of NMC622, carbon black C65, and PVDF in NMP was cast on a polyethylene terephthalate (PET) film and the electronic conductivity of the cathode film was measured. The electrical conductivities of the uncalendered cathodes are 9.8, 7.0, 2.7 to 1.0 S m^{-1}, respectively, for formulations of 94:4:2 to 97:1:2, as shown in Figure 6b.

Generally, the electrical conductivity could be improved through calendering by decreasing the porosity and increasing the tortuosity.[45] The relationship between electrical conductivity and tortuosity/porosity can be described by the MacMullin number (N_M), as shown in Equation (3)

$$N_M = \frac{\sigma_{eff}}{\sigma_0} = \frac{\tau}{\varepsilon} \tag{3}$$

where σ_{eff} is the effective conductivity; σ_0 is the intrinsic conductivity; τ is the tortuosity; and ε is the porosity.

Calendering results in a decrease in porosity and an increase in tortuosity. Thus, the value of N_M increases, and the effective conductivity becomes larger as indicated in Equation (3). This is in agreement with several other studies that show that calendering affects electrical conductivity.[45] However, some literature demonstrated that calendering influences the electrical conductivity of the NMC cathodes very slightly.[46,47] To provide further clarity on this problem, we conducted additional experiments and subsequently presented a more comprehensive discussion in the following. The cathode films based on formulations of 97:1:2, 96:2:2, 95:3:2, and 94:4:2 were calendered from a thickness of 0.060, 0.074, 0.079, and 0.059 mm (porosity about 50 %) to 0.049, 0.066, 0.057, and 0.045 mm (porosity about 40%) and the corresponding electrical conductivities were 0.3, 1.3, 6.9, and 6.5 S m^{-1}, respectively. The electrical conductivities of all the films become smaller after calendering. The percentage change between the conductivity of calendered and uncalendared electrodes is 33.7%, 1.4%, 51.9%, and 70.0% for the coating film with the formulation of 94:4:2, 95:3:2, 96:2:2, and 97:1:2, respectively.

The electrical conductivity of the calendered film is smaller than that without calendering, as shown in Figure 6b. One

possible reason is that the CBD conductivity is strain-dependent,[9,48] and the conductivity decreases with an increase in strain caused by calendering. Another possible reason is that the conductivity is tortuosity-dependent. In some cases, although the tortuosity is increased through calendering, the electrical conductivity still decreases. This was demonstrated by Trembacki et al. through simulation.[49] It may also be related to the recent discovery that calendering causes particle redistribution of the CBD.[50] The third possible reason is that calendering may break down the connection between active material particles and the CBD. Lu et al. pointed out that calendering a thin electrode has a higher chance to generate cracks between the CBD and active material particle surface thus undermining electronic percolation and reaction homogeneity.[51]

Finally, we propose that there are two "nested" percolation systems for the CBD in LIB electrodes. The first percolation system involves carbon black dispersed in PVDF, forming an electrically conductive polymer CBD structure in the electrode as the basis for electrode electronic conduction. The secondary percolation system is an electrically conductive polymer structure with pores dispersed in the space among NMC622 particles, forming an electrically conductive electrode. With increasing carbon black content in either the first percolation system or the secondary percolation system, the electrical conductivity improves correspondingly.

2.6. Pore Size Distribution and Two-Nested Pore Systems for CBD in the LIB Electrode

The ionic conductivity (κ) and ionic diffusivity (D) in LIBs are determined by the pore tortuosity. The equations are listed as follows

$$\kappa = \kappa_0 \left(\frac{\varepsilon}{\tau}\right)^b \text{ and } D = D_0 \left(\frac{\varepsilon}{\tau}\right)^b \tag{4}$$

where κ_0 and D_0 are the free constant ionic conductivity and constant ionic diffusivity, respectively; b is a constant coefficient. Therefore, the pore distribution highly influences the Li-ion diffusion in the porous electrode.

Through characterization by mercury intrusion porosimetry (MIP) of uncalendered electrodes, it reveals that the pore size distribution of the prepared electrodes showed two peaks, as shown in **Figure 7**a. The first peak is situated at a size of

ADVANCED
SCIENCE NEWS
www.advancedsciencenews.com

Energy Technology
Generation, Conversion, Storage, Distribution
www.entechnol.de
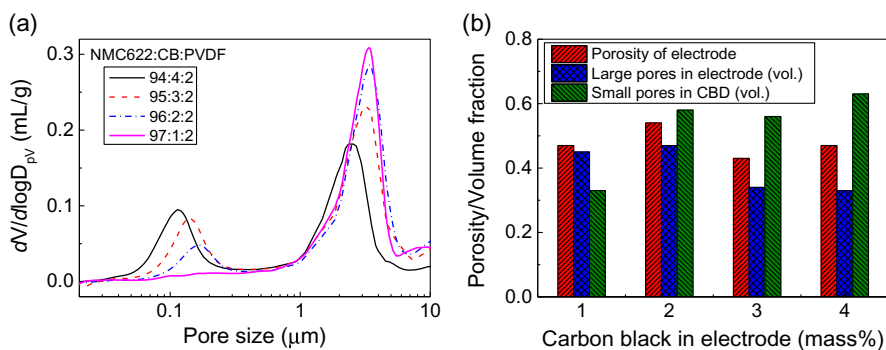
Figure 7. a) Pore size distribution measured using MIP showing changes in CBD pore size as additive content increases. b) Data extracted show overall porosity, CBD small pore, and electrode large pore volume fraction.

≈100 nm, which corresponds to small pores of carbon black aggregates in PVDF. These pores are formed in the period of the first percolation and are known as the pores in CBD. The small pore sizes are 115, 140, 165, and 227 nm for the electrodes based on the formulation of 94:4:2, 95:3:2, 96:2:2, and 97:1:2, respectively. The second peak is located at a size of ≈3.0 μm, which corresponds to the large pores among the NMC622 particles formed during the second percolation. The large pore sizes are 2.5, 3.2, 3.4, and 3.4 μm for the electrodes based on the formulation of 94:4:2, 95:3:2, 96:2:2, and 97:1:2, respectively. This result is also demonstrated by Bockholt et al.,[27] Mayer et al.,[41] and Mayer et al.[52] They reported findings of carbon black aggregate pores with a size of around 80–100 nm and NMC622 pores with a size of around 3 μm. The pore size distribution curves also show that with decreasing carbon black, the two-peak curve becomes an almost single-peak curve as the first peak nearly disappears. We infer that this is due to an increase in the binder-to-carbon black ratio which results in a decrease in bridge structures, and a change to the film structure as the quantity of carbon black decreases with the formulation from 94:4:2, 95:3:2, 96:2:2 to 97:1:2, respectively. The schematic diagrams of these structural changes are shown in Figure 3i–l. Meyer et al. and Beuse et al. demonstrated that with calendering, the two peaks shift to the left with smaller pore sizes and lower peak height.[53,54] Therefore, it may be more meaningful to compare the performance of LIBs with the pore distributions with uncalendered electrodes because this enables us to clearly distinguish the small pores in the CBD and large pores in the electrode and evaluate the influence of tape casting and drying on the formation of the original pore distribution.

Through calculation,[55] the porosity of the electrode (red), the volume fractions of large pores in the electrode (blue), and small pores in CBD (green) are shown in Figure 7b corresponding to the pores in Figure 7a with uncalendered electrode. Among these formulations, the highest volume fraction of large pores within the electrode and the lowest volume fraction of small pores in the CBD is from the formulation of 97:1:2. On the contrary, the lowest volume fraction of large pores (≈3.0 μm) in the electrode and the highest volume fraction of small pores (≈100 nm) in the CBD is from the formulation of 94:4:2. As the pore size and pore tortuosity can significantly influence Li-ion diffusion and the volume fraction of small pores (≈100 nm) in the CBD is dominant of controlling the charge transfer between liquid electrolyte and

the surface of active material particle, Figure 7b offers some insights indicating the electrode based on the formulation of 94:4:2 has the lowest charge transfer resistance due to Equation (4). The variation trend of the volume of small pores in CBD (green) in Figure 7b matches the variation trend of the first peak height and area in Figure 7a, but it is also influenced by the porosity of the electrode (red).

The large pores in the electrodes and small pores in CBD highly influence the Li-ion diffusion and the impedance of the electrode. Kroll et al. revealed that pores limit Li-ion transport through tortuous and constricted diffusion pathways.[56] Hein et al. provided a link between spatial CBD distribution and electrode impedance.[31] Therefore, the pore distribution is crucial to the performance of the CBD.

To investigate the effect of pore size on charge transfer, electrochemical impedance spectroscopy (EIS) was used to determine the charge transfer resistance at the interface and Li-ion diffusion. The Nyquist plots for the impedances of electrodes and the equivalent circuit are shown in **Figure 8**. In the equivalent circuit, R_s is the resistance for the electrolyte solution; R_{cf} is the charge transfer resistance; CPE_{dl} is the constant phase element for the double layer; and CPE_{diff} is the constant phase element for diffusion. The equivalent circuit is similar to that from the study of Chen et al.[57] Calendering shifts the pore distribution curves to the left so the EIS measurement uses the calendered electrodes based on four formulations and a half-coin cell with Li metal as the counter electrode. The charge transfer resistances (R_{cf}) are 33.6, 45.5, 90.8 to 103.0 Ω corresponding to the electrodes based on the formulations of 94:4:2, 95:3:2, 96:2:2, and 97:1:2, respectively. It indicates that the charge transfer resistance decreases with increasing the carbon black content and volume fraction of small pores in the CBD. It highlights that the pore volume in the CBD is critical for Li-ion transfer and generally increasing the volume of pores in the CBD can enhance the Li-ion transfer.

The experiments reveal that there are two "nested" pore systems in the electrode: the first pore system is small pores in the CBD, forming charge transfer between the surface of active material particles and liquid electrolyte in the large pores; the second pore system is large pores in the electrode, forming the channels for Li-ion diffusion in the porous electrodes. By increasing the volume of small pores in CBD, the charge transfer resistance decreases correspondingly.
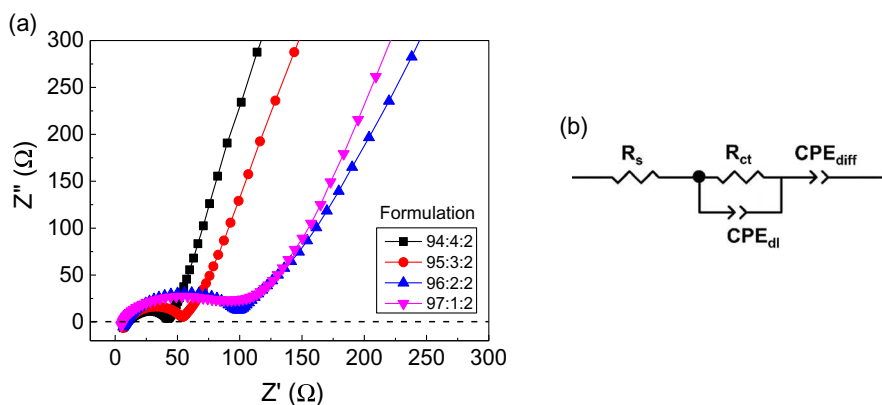
Figure 8. EIS of the electrodes a) impedance; b) equivalent circuit.

2.7. Relationship of Percolation Systems and Pore Systems in the LIB Electrode

The percolation system in the electrode controls the electron transfer while the pore system in the electrode controls the Li-ion diffusion in the electrolyte. Electron transfer and Li-ion diffusion are intrinsically linked. From Equations (5) and (6) of open-circuit potential and overpotential derived by Drummond et al.,[18] there is an important parameter, $\sigma/(\sigma + \kappa)$, which unveils their intrinsic relations.

$$V_{oc}(t) = U(c_s^{surf}(x = 0, t)) + \int_0^L \left(\frac{\sigma(x)}{\sigma(x) + \kappa(x)} \right) \times \left(\frac{\partial U(c_s^{surf}(x, t))}{\partial x} \right) dx \quad (5)$$

$$V_{op}(t) = \eta(x = 0, t) + \int_0^L \left(\frac{\sigma(x)}{\sigma(x) + \kappa(x)} \right) \times \left(\frac{\partial \eta(x, t)}{\partial x} \right) dx \quad (6)$$

If n is defined as $n = \sigma/\kappa$, the relationship between h and n is shown below.

$$h = \frac{\sigma}{\sigma + \kappa} = \frac{1}{1 + \frac{1}{n}} \quad (7)$$

It is shown that when n is greater than 10, h approaches 1. This illustrates that when the electrical conductivity is greater than the ionic conductivity by a factor of ten, there is only a slight improvement in battery performance by further increasing the electrical conductivity. The validation and examination of this relation were demonstrated by Drummond et al.[18] and have therefore been omitted in this section to avoid repetitive and lengthy descriptions. Drummond et al. demonstrated that the highest reactivity occurs close to the separator and the overpotential reaches the highest value (3.0–3.5 V) near the separator with $n \geq 10$.[18] Generally, the local ionic conductivity in the electrode is between 0.1 and 1 S m^{-1},[18,57,58] e.g., typically 0.5 S m^{-1} which means when the electrical conductivity is greater than 5 S m^{-1}, the rate performance improvement of the battery is very limited. Moreover, Zhang et al. pointed out that the effective ionic conductivity for liquid electrolyte may be lower than 10^{-2} S m^{-1} because the transfer number of Li-ion is less than 0.5.[58] In this

case, one possible approach is to find a way to further increase the ionic conductivity to improve the battery performance. Improving the performance of the battery is only achievable when the ionic conductivity is improved and coupled with increasing electrical conductivity.

There is a relationship between ionic conductivity and ionic diffusivity, as shown in Equation (8).[16] Therefore, in essence, ion conduction is controlled by ion diffusion.

$$\kappa = \frac{q_i^2 c_i}{k_B T} D_i \quad (8)$$

Consequently, it is a synergy mechanism in which electron transfer and Li-ion diffusion collaboratively work together. Because of that, both the percolation system and pore system should be considered together for the CBD design. This highlights the relationship between electron transfer and ion diffusion and emphasizes why electron transfer is limited by ion diffusion.

2.8. Galvanostatic Cycling

To investigate the effect of the quantity of carbon black and CBD on the battery performance, all the NMC622 electrodes were calendered according to traditional industrial manufacturing procedures. The electrodes and coin half cells were prepared based on the formulations of 94:4:2, 95:3:2, 96:2:2, and 97:1:2, respectively. The dimensions and parameters of these electrodes are listed in **Table 1**.

The charge–discharge curves for the electrodes based on different formulations are shown in **Figure 9**. These curves follow the particle bipolarization mechanism with intermediate, delithiated/lithiated, and Li-poor/Li-rich phases.[59] Changing the charge/discharge conditions changes the slope and shape of the end arches.[59] The capacity decreases as the cell is charged or discharged with increasing C-rates.

The rate capabilities for the electrodes are shown in **Figure 10**. With increasing carbon black content from the formulation of 97:1:2 to 94:4:2, the capacities are similar when C-rates below 1 C. However, the capacities start to increase under high C-rates, such as 2 C and 5 C. For example, the electrode based on the formulations of 94:4:2 and 95:3:2 achieved around 10 mAh g^{-1} at 5 C, but the capacities for the electrodes based on the

**ADVANCED
SCIENCE NEWS**

www.advancedsciencenews.com

Energy Technology
Generation, Conversion, Storage, Distribution

www.entechnol.de

Table 1. Electrode parameters of coin half-cell fabricated from different formulations.

Formulation	Diameter [mm]	Thickness [mm]	Mass [mg]	Area mass [g m^{-2}]	Porosity before calendering	Porosity after calendering	Capacity [mAh cm^{-2}]	C-rate [mAh]
94:4:2	14.8	0.103 (0.084)[a]	41.36	199	0.47	0.32	3.35	5.63
95:3:2	14.8	0.104 (0.086)[a]	45.10	221	0.43	0.28	3.71	5.82
96:2:2	14.8	0.102 (0.073)[a]	37.80	178	0.54	0.30	3.00	5.15
97:1:2	14.8	0.096 (0.078)[a]	40.11	192	0.47	0.32	3.23	5.60

[a]Thickness after calendering.
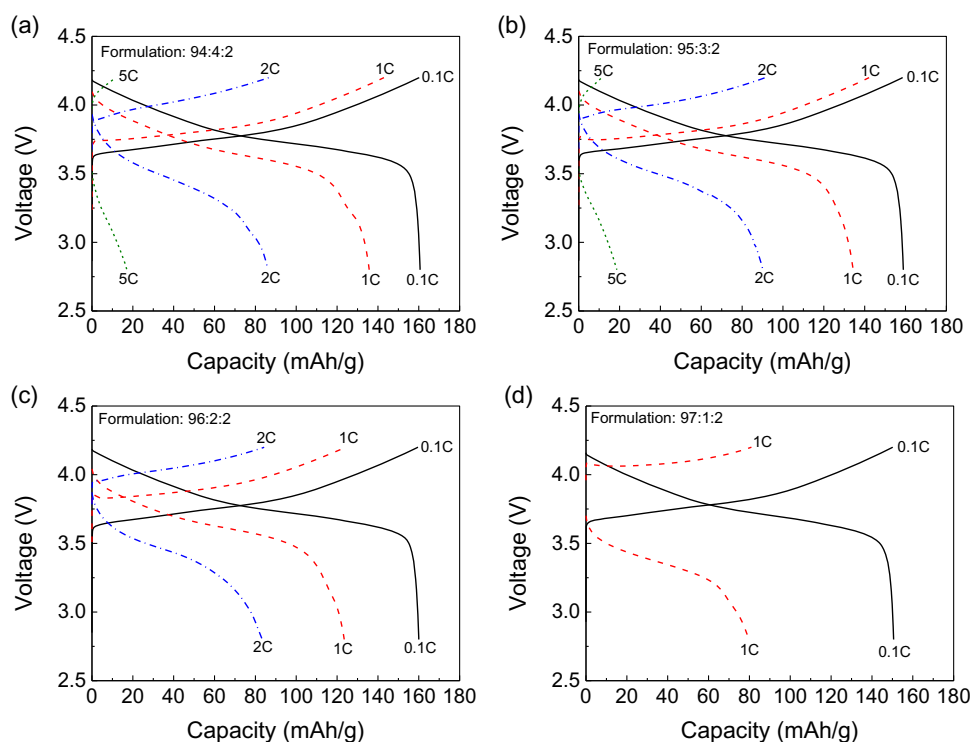
Figure 9. Charge–discharge curves for the calendered cathodes based on different electrode formulations. a–d) 94–97 wt% active material, respectively.
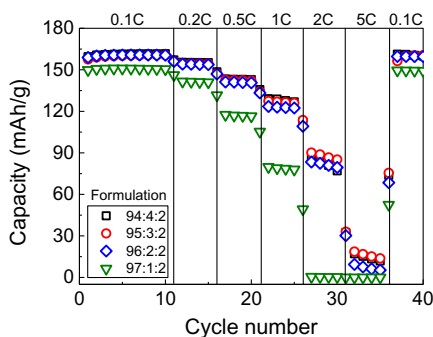
Figure 10. Rate capabilities for the calendered cathodes based on different electrode formulations.

formulations of 96:2:2 and 97:1:2 approached 0 at 5 C. Even under 2 C, the capacity of the electrode based on the formulation of 97:1:2 reaches 0. With increasing carbon black content, the electrical conductivity and volume of pores in CBD increase. The charge transfer resistance decreases with increasing carbon black content and volume fraction of small pores in the CBD. As a result, the rate capability is improved.

Further analysis is shown in **Figure 11**. For the first percolation system, as shown in Figure 11a, the volume fraction of carbon black in PVDF rises from 35.7, 52.7, 62.5 to 69.0% corresponding to the formulation of 97:1:2, 96:2:2, 95:3:2, and 94:4:2, respectively. For the C-rate performance at 5 C, the capacity improves from 0 to 11.1 mAh g^{-1} when the volume fraction of carbon black in PVDF elevates from 35.7 to 62.5% but the
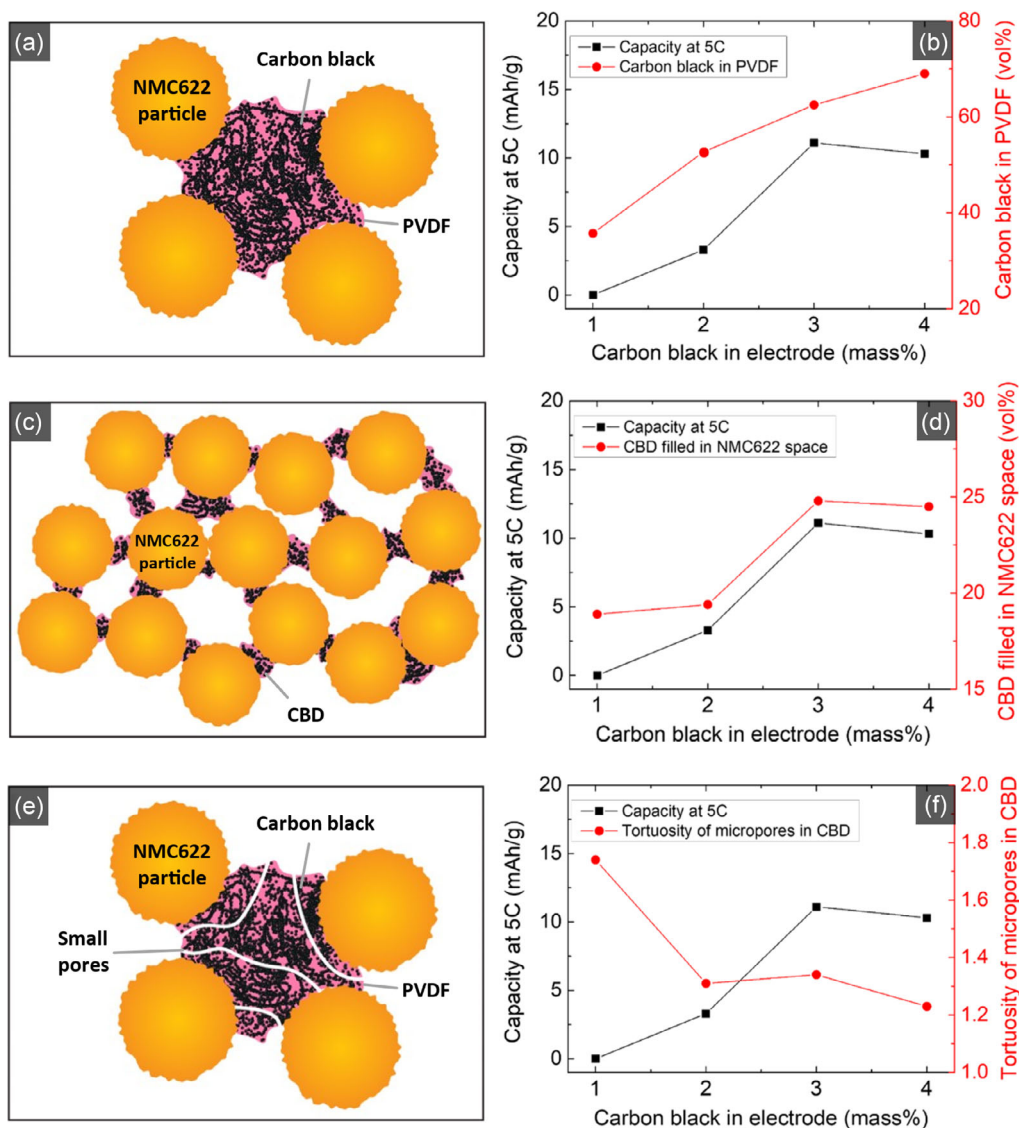
Figure 11. A model with two percolation systems for CBD structures in electrodes. a) First system: carbon black dispersed in the PVDF; b) Relationship of carbon black in PVDF and capacity at 5 C under different carbon black mass contents; c) Second system: carbon black-PVDF polymer structure dispersed in the space among active material particles; d) The relationship of CBD in the space among active material particles and capacity at 5 C; e) Small pores in the first percolation CBD system; f) The relationship of the volume of small pores in CBD and capacity at 5 C.

capacity drops slightly to 10.3 mAh g^{-1} as the carbon black volume in PVDF reaches 69.0%. The result is shown in Figure 11b. The trend of rate performance matches the trend of the volume fraction of carbon black in PVDF, which indicates the trend of electrical conductivity. For the second percolation system, as shown in Figure 11c, the CBD volume fraction (the volume of carbon black and PVDF excluding the volume of small pores) in the space among NMC622 particles increases from 18.9, 19.4 to 24.8% corresponding to the formulation of 97:1:2. 96:2:2 and 95:3:2, respectively, and simultaneously, the capacity at 5 C increases from 0 to 11.1 mAh g^{-1}. Furthermore, as the CBD volume fraction declines to 24.5%, the capacity falls to 10.3 mAh g^{-1}, as shown in Figure 11d. This indicates that the C-rate performance of LIBs is strongly related to the volume

fraction of the CBD in the space among NMC622 particles. A higher CBD volume fraction can create larger channels for electron transfer to the current collector. The conductivity measured by the four-point method only reflects the electron transfer along the electronic short-range chain inside the electrode but does not reflect the electron transfer status along the electronic long-range chain to the current collector. This means that the measured conductivity increases (Figure 6b) but the rate performance decreases from the formulation of 95:3:2 to 94:4:2. Therefore, a higher volume of CBD structure is beneficial for the electron transfer to the current collector. When the volume fraction of the CBD reaches the maximum value of about 25%, which is equivalent to a volume fraction of carbon black in PVDF higher than 50% in this work, the optimal rate performance is achieved. For

our studied cases, the formulation of 95:3:2 is optimal, as shown in Figure 11d.

There are pores in CBD structures of the first percolation system which are the composites formed by carbon black dispersed in PVDF, as shown in Figure 11e. These pores in the CBD structure affect the Li-ion diffusion significantly. If the porosity approaches 0, it is impossible for Li-ions to penetrate the CBD structures. For example, in the electrode based on the formulation of 97:1:2, very few pores are formed in the CBD structures, and it displays the worst rate performance. According to the MacMullin number equation (Equation (3)), the migration of Li-ions in the CBD structures is determined by the porosity and pore structure such as tortuosity. The comparison of the trend of capacity at 5 C and the CBD tortuosity for different formulations is shown in Figure 11f. The tortuosity of CBD is obtained from the Bruggeman model as

$$\tau = \varepsilon^{-0.5} \tag{9}$$

The volume fraction of small pores in CBD is 0.33, 0.58, 0.56, 0.66 and its tortuosity is 1.74, 1.31, 1.34, 1.23, respectively, for the electrodes based on the formulations of 97:1:2, 96:2:2, 95:3:2 and 94:4:2. From Figure 11f, it is known that the trend of the rate performance is essentially in the opposite direction of the trend of CBD tortuosity. In this work, the mass ratio of carbon black to PVDF of more than 1:1 is favorable for increasing rate performance. This conclusion is different from previous studies.[60,61] The free PVDF with a mass ratio of carbon black to PVDF less than 1:1 is beneficial to the performance of LIBs.

In summary, the rate performance of LIBs based on NMC622 is closely linked to the volume fraction of CBD in the space between active material particles.

3. Conclusion

The purpose of this article is to explore the structure and mechanism of the CBD long-range electrical conduction and to improve the LIB performance through designing the CBD and optimizing formulation for next-generation NMC622 LIBs. We draw the following conclusions and findings: 1) There are two main CBD structures in NMC622 LIBs for long-range electronic contacts: film structures located on the surface of active material particles and bridge structures which cross over two adjacent active material particles. A higher number of bridge structures are beneficial to electronic conduction; 2) There are two "nested" percolation systems in the electrode for long-range electrical conduction: the first percolation system is carbon black dispersed in PVDF; the second percolation system is the carbon black-PVDF polymer structure dispersed in the space among active material particles. It was demonstrated that the electrical conductivity is elevated as the carbon black content in PVDF is increased. The experimental results showed the highest volume fraction of the CBD in the space among active material particles achieved the best rate performance of the electrode; 3) There are two "nested" pore systems in the electrode for Li-ion transfer: The first pore system is the small pores (e.g., 100 nm) in the CBD formed during the first percolation; The second pore system is the large pores (e.g., 3 μm) in the electrode formed during

the second percolation. The porosity and tortuosity of CBD have an impact on local Li-ion diffusion. Higher internal CBD porosity (>0.56) and smaller tortuosity (<1.34) of CBD are favorable for rate performance. The interplay between small pores in the CBD and large pores in the electrode impacts the performance of LIBs; and 4) The improvement of battery performance through increasing the electrical conductivity (σ) is limited by the CBD pore systems for the ionic conductivity (κ) and diffusivity (D). The electron transfer and Li-ion transfer work collaboratively for LIBs. It demonstrated that when $\sigma/\kappa \geq 10$, the electrical conductivity influences the rate performance of LIBs very limitedly. In this case, the focus lies on increasing the Li-ion diffusion in the electrolyte. Therefore, the design and construction of microstructure in CBD should also establish the two percolation systems and two pore systems together.

The electrochemistry of the NMC622 electrode is more of a long-range electronic conduction-controlled and Li-ion diffusion-controlled process. Therefore, the improvement of the rate capabilities of LIBs based on NMC622 should involve increasing electron and Li-ion transfer together by constructing two "nested" percolation systems and two "nested" pore systems. Finally, based on this work, the optimal formulation of 95:3:2 is proposed.

Conflict of Interest

The authors declare no conflict of interest.

Data Availability Statement

The data that support the findings of this study are available from the corresponding author upon reasonable request.

[1] S. N. Bryntesen, A. H. Strømman, I. Tolstorebrov, P. R. Shearing, J. J. Lamb, O. S. Burheim, *Energies* **2021**, *14*, 1406.
[2] Y. Zhao, P. Stein, Y. Bai, M. Al-Siraj, Y. Yang, B.-X. Xu, *J. Power Sources* **2019**, *413*, 259.
[3] W. B. Hawley, J. Li, *J. Energy Storage* **2019**, *25*, 100862.

[4] J. Li, J. Fleetwood, W. B. Hawley, W. Kays, *Chem. Rev.* **2022**, *122*, 903.

[5] A. Gomez-Martin, F. Reissig, L. Frankenstein, M. Heidbüchel, M. Winter, T. Placke, R. Schmuch, *Adv. Energy Mater.* **2022**, *12*, 2103045.

[6] G. E. Blomgren, *J. Electrochem. Soc.* **2017**, *164*, A5019.

[7] M. Zybert, H. Ronduda, A. Szczęsna, T. Trzeciak, A. Ostrowski, E. Żero, W. Wieczorek, W. Raróg-Pilecka, M. Marcinek, *Solid State Ion.* **2020**, *348*, 115273.

[8] J. R. Croy, A. Abouimrane, Z. Zhang, *MRS Bull.* **2014**, *39*, 407.

[9] M. E. Ferraro, B. L. Trembacki, V. E. Brunini, D. R. Noble, S. A. Roberts, *J. Electrochem. Soc.* **2020**, *167*, 013543.

[10] H. Gao, Q. Wu, Y. Hu, J. P. Zheng, K. Amine, Z. Chen, *J. Phys. Chem. Lett.* **2018**, *9*, 5100.

[11] R. Tian, N. Alcala, S. J. K. O'Neill, D. V. Horvath, J. Coelho, A. J. Griffin, Y. Zhang, V. Nicolosi, C. O'Dwyer, J. N. Coleman, *ACS Appl. Energy Mater.* **2020**, *3*, 2966.

[12] T. V. S. L. Satyavani, B. R. Kiran, V. R. Kumar, A. S. Kumar, S. V. Naidu, *Eng. Sci. Technol. Int. J.* **2016**, *19*, 40.

[13] R. Amin, Y.-M. Chiang, *J. Electrochem. Soc.* **2016**, *163*, A1512.

[14] Y. Orikasa, Y. Gogyo, H. Yamashige, M. Katayama, K. Chen, T. Mori, K. Yamamoto, T. Masese, Y. Inada, T. Ohta, Z. Siroma, S. Kato, H. Kinoshita, H. Arai, Z. Ogumi, Y. Uchimoto, *Sci. Rep.* **2016**, *6*, 26382.

[15] G. Kucinskis, G. Bajars, J. Kleperis, *J. Power Sources* **2013**, *240*, 66.

[16] M. Park, X. Zhang, M. Chung, G. B. Less, A. M. Sastry, *J. Power Sources* **2010**, *195*, 7904.

[17] S. Mousavihashemi, K. Lahtinen, T. Kallio, *Electrochim. Acta* **2022**, *412*, 140093.

[18] R. Drummond, C. Cheng, P. S. Grant, S. R. Duncan, *J. Electrochem. Soc.* **2022**, *169*, 010528.

[19] K. R. Tallman, G. P. Wheeler, C. J. Kern, E. Stavitski, X. Tong, K. J. Takeuchi, A. C. Marschilok, D. C. Bock, E. S. Takeuchi, *J. Phys. Chem. C* **2021**, *125*, 58.

[20] J. Entwistle, R. Ge, K. Pardikar, R. Smith, D. Cumming, *Renewable Sustainable Energy Rev.* **2022**, *166*, 112624.

[21] R. M. Saraka, S. L. Morelly, M. H. Tang, N. J. Alvarez, *ACS Appl. Energy Mater.* **2020**, *3*, 11681.

[22] S. Yari, H. Hamed, J. D'Haen, M. K. Van Bael, F. U. Renner, A. Hardy, M. Safari, *ACS Appl. Energy Mater.* **2020**, *3*, 11820.

[23] D. Parikh, T. Christensen, J. Li, *J. Power Sources* **2020**, *474*, 228601.

[24] S. L. Morelly, N. J. Alvarez, M. H. Tang, *J. Power Sources* **2018**, *387*, 49.

[25] R. Dominko, M. Gaberscek, J. Drofenik, M. Bele, S. Pejovnik, J. Jamnik, *J. Power Sources* **2003**, *119–121*, 770.

[26] M. Wang, D. Dang, A. Meyer, R. Arsenault, Y.-T. Cheng, *J. Electrochem. Soc.* **2020**, *167*, 100518.

[27] H. Bockholt, W. Haselrieder, A. Kwade, *Powder Technol.* **2016**, *297*, 266.

[28] W. Bauer, D. Nötzel, V. Wenzel, H. Nirschl, *J. Power Sources* **2015**, *288*, 359.

[29] B. L. Trembacki, D. R. Noble, V. E. Brunini, M. E. Ferraro, S. A. Roberts, *J. Electrochem. Soc.* **2017**, *164*, E3613.

[30] I. Srivastava, D. S. Bolintineanu, J. B. Lechman, S. A. Roberts, *ACS Appl. Mater. Interfaces* **2020**, *12*, 34919.

[31] S. Hein, T. Danner, D. Westhoff, B. Prifling, R. Scurtu, L. Kremer, A. Hoffmann, A. Hilger, M. Osenberg, I. Manke, M. Wohlfahrt-Mehrens, V. Schmidt, A. Latz, *J. Electrochem. Soc.* **2020**, *167*, 013546.

[32] C. D. Reynolds, P. R. Slater, S. D. Hare, M. J. H. Simmons, *Mater. Des.* **2021**, *209*, 109971.

[33] W. Bauer, D. Nötzel, *Ceram. Int.* **2014**, *40*, 4591.

[34] B. Zhao, D. Yin, Y. Gao, J. Ren, *Ceram. Int.* **2022**, *48*, 19073.

[35] L. Ouyang, Z. Wu, J. Wang, X. Qi, Q. Li, J. Wang, S. Lu, *RSC Adv.* **2020**, *10*, 19360.

[36] M. Nikpour, B. Liu, P. Minson, Z. Hillman, B. A. Mazzeo, D. R. Wheeler, *Batteries* **2022**, *8*, 107.

[37] F. Ma, Y. Fu, V. Battaglia, R. Prasher, *J. Power Sources* **2019**, *438*, 226994.

[38] S. H. Sung, *PhD Thesis*, Seoul National University, South Korea, **2019**.

[39] Y. S. Zhang, N. E. Courtier, Z. Zhang, K. Liu, J. J. Bailey, A. M. Boyce, G. Richardson, P. R. Shearing, E. Kendrick, D. J. L. Brett, *Adv. Energy Mater.* **2022**, *12*, 2102233.

[40] P. Bacchin, D. Brutin, A. Davaille, E. D. Giuseppe, X. D. Chen, I. Gergianakis, F. Giorgiutti-Dauphiné, L. Goehring, Y. Hallez, R. Heyd, R. Jeantet, C. L. Floch-Fouéré, M. Meireles, E. Mittelstaedt, C. Nicloux, L. Pauchard, M.-L. Saboungi, *Eur. Phys. J. E* **2018**, *41*, 94.

[41] J. K. Mayer, H. Bockholt, A. Kwade, *J. Power Sources* **2022**, *529*, 231259.

[42] J.-C. Huang, *Adv. Polym. Technol.* **2002**, *21*, 299.

[43] P. J. Brigandi, J. M. Cogen, R. A. Pearson, *Polym. Eng. Sci.* **2014**, *54*, 1.

[44] G. Liu, H. Zheng, X. Song, V. S. Battglia, *J. Electrochem. Soc.* **2012**, *159*, A214.

[45] J. Zhang, H. Huang, J. Sun, *Powder Technol.* **2022**, *409*, 117828.

[46] H. Zheng, G. Liu, X. Song, R. Ridgway, S. Xun, V. S. Battaglia, *J. Electrochem. Soc.* **2010**, *157*, A1060.

[47] E. E. Hunter, *Master Thesis*, Brigham Young University, USA, **2020**.

[48] J. Krajči, Z. Špitálský, I. Chodák, *Eur. Polym. J.* **2014**, *55*, 135.

[49] B. L. Trembacki, A. N. Mistry, D. R. Noble, M. E. Ferraro, P. P. Mukherjee, S. A. Roberts, *J. Electrochem. Soc.* **2018**, *165*, E725.

[50] M. J. Lain, E. Apachitei, L. Román-Ramírez, M. Copley, J. Marco, *Phys. Chem. Chem. Phys.* **2022**, *24*, 29999.

[51] X. Lu, S. R. Daemi, A. Bertei, M. D. R. Kok, K. B. O'Regan, L. Rasha, J. Park, G. Hinds, E. Kendrick, D. J. L. Brett, P. R. Shearing, *Joule* **2020**, *4*, 2746.

[52] J. K. Mayer, L. Almar, E. Asylbekov, W. Haselrieder, A. Kwade, A. Weber, H. Nirschl, *Energy Technol.* **2020**, *8*, 1900161.

[53] C. Meyer, H. Bockholt, W. Haselrieder, A. Kwade, *J. Mater. Process. Technol.* **2017**, *249*, 172.

[54] T. Beuse, M. Fingerle, C. Wagner, M. Winter, M. Börner, *Batteries* **2021**, *7*, 70.

[55] R. Ge, A. M. Boyce, Y. Sun, P. R. Shearing, P. S. Grant, D. J. Cumming, R. M. Smith, *ACS Appl. Mater. Interfaces* **2023**, *15*, 27809.

[56] M. Kroll, S. L. Karstens, M. Cronau, A. Höltzel, S. Schlabach, N. Nobel, C. Redenbach, B. Roling, U. Tallarek, *Batter. Supercaps* **2021**, *4*, 1363.

[57] C.-H. Chen, F. B. Planella, K. O'Regan, D. Gastol, W. D. Widanage, E. Kendrick, *J. Electrochem. Soc.* **2020**, *167*, 080534.

[58] Y. Zhang, Z. Zheng, X. Liu, M. Chi, Y. Wang, *J. Electrochem. Soc.* **2019**, *166*, A515.

[59] A. Haghipour, M. Tahertalari, M. M. Kalantarian, *Sustainable Energy Fuels* **2022**, *6*, 879.

[60] H. Zheng, R. Yang, G. Liu, X. Song, V. S. Battaglia, *J. Phys. Chem. C* **2012**, *116*, 4875.

[61] G. Liu, H. Zheng, A. S. Simens, A. M. Minor, X. Song, V. S. Battaglia, *J. Electrochem. Soc.* **2007**, *154*, A1129.